AIMS Mathematics, 11(9): 29560–29586.
DOI: 10.3934/math.20261173
Received: 08 May 2026
Revised: 22 August 2026
Accepted: 08 September 2026
Published: 14 September 2026

https://www.aimspress.com/journal/Math

Research article

Numerical approximation of an initial–boundary value problem for a variable-coefficient hyperbolic Schrödinger equation

Muhammed Hasdemir*

Aydın Vocational School of Health Services, Aydın Adnan Menderes University, Aydın, Türkiye

* **Correspondence:** Email: muhammed.hasdemir@adu.edu.tr.

Abstract: We study an initial–boundary value problem for a three-dimensional variable-coefficient hyperbolic Schrödinger equation whose spatial operator has an indefinite structure. Under suitable regularity and positivity assumptions on the variable coefficient, a uniqueness result is first established for the continuous problem. The main contribution is the development and analysis of a Crank–Nicolson finite difference scheme combining trapezoidal time averaging with second-order central spatial differences. The method leads to a sparse complex linear system at each time step, with a time-independent coefficient matrix that allows a single factorization to be reused. The local truncation error is of second order in both time and space. A frozen-coefficient von Neumann analysis gives an amplification factor of unit modulus. For the variable-coefficient Dirichlet problem, a discrete weighted-energy argument establishes conservation of the weighted norm for the homogeneous perturbation equation and yields stability and second-order convergence without a time-step restriction. Numerical experiments based on two manufactured solutions examine spatial and temporal convergence separately. The errors decrease under refinement and generally support the predicted behavior, although the more oscillatory second example exhibits somewhat lower spatial convergence rates. Monte Carlo simulations with additive complex Gaussian noise further assess the sensitivity of the computed solutions to perturbations in the input data. These results provide a numerical framework for the considered variable-coefficient hyperbolic Schrödinger problem.

Keywords: initial–boundary value problem; hyperbolic Schrödinger equation; Crank–Nicolson scheme; finite difference method; Von Neumann stability; convergence analysis
Mathematics Subject Classification: 65M06, 65M12, 65M15, 35Q41

1. Introduction

Schrödinger-type partial differential equations constitute one of the most important model classes in modern mathematical physics. Since they describe the space–time evolution of complex-valued

wave functions, these equations play a central role in both theoretical and applied studies [1]. In quantum mechanics, the Schrödinger equation serves as a fundamental tool for describing the behavior of microscopic physical systems and the temporal evolution of the probability amplitudes of particles, and it remains one of the fundamental models of quantum theory, [1–3]. In addition, this class of equations is widely used in optics for the study of the propagation of light in dispersive and nonlinear media, fiber-optic systems, and the evolution of wave packets [4,5], in wave dynamics for the modeling of evolution processes dominated by dispersive effects [3, 5], and in Bose–Einstein condensates for explaining macroscopic quantum behavior and the dynamics of condensed phases [6].

In this study, we consider the following Schrödinger equation defined on a bounded rectangular region $\Omega \subset \mathbb{R}^3$:

$$\mathcal{S}z(t, \mathbf{x}) = f(t, \mathbf{x}), \qquad (t, \mathbf{x}) \in \Omega_T, \tag{1.1}$$

where $T > 0$ is a fixed final time, $\Omega_T := \Omega \times (0, T)$, $\mathbf{x} = (x_1, x_2, y)$, and $\mathcal{S}$ is the Schrödinger operator defined by

$$\mathcal{S} := \partial_t + ia^{-1}\mathcal{L}, \qquad \mathcal{L} := \partial_y^2 - \partial_{x_1}^2 - \partial_{x_2}^2, \tag{1.2}$$

Here, $i = \sqrt{-1}$ denotes the imaginary unit. Furthermore, $a = a(x_1, x_2)$ is a sufficiently smooth and strictly positive coefficient function depending on the spatial variables, f is the given source term, and $z : [0, T] \times \overline{\Omega} \to \mathbb{C}$ is the unknown complex-valued solution function. Since the spatial operator $\mathcal{L}$ defined by (1.2) contains a positive second derivative in the y-direction and negative second derivatives in the x_1- and x_2-directions, it has an indefinite (hyperbolic) character; therefore, equation (1.1) is referred to in the literature as a hyperbolic Schrödinger equation [7–9].

The mathematical analysis of Schrödinger equations is an intensive area of research. For the classical constant-coefficient Schrödinger equation, fundamental properties such as well-posedness of the Cauchy problem, regularity, and dispersive behavior have been studied systematically in standard references [2]; see also [10] for related developments in other classes of evolution equations. In recent years, attention has shifted toward more general Schrödinger operators whose coefficients depend on the spatial or temporal variables. In this context, Junior et al. [3] studied the Cauchy problem for Schrödinger operators involving singular lower-order terms within the framework of very weak solutions, while Federico, Li, and Yu [5] obtained results concerning uniqueness and unique continuation for variable-coefficient Schrödinger equations. These studies show that the variable-coefficient structure requires a significantly more delicate analytical framework than the classical constant-coefficient case.

Schrödinger problems whose spatial operator has an indefinite character are of particular importance within this general class. Barceló, Cassano, and Fanelli [7] obtained results on unique continuation properties and Gaussian-type lower bounds for Schrödinger equations involving a hyperbolic Laplace operator from data at a single time. Such results demonstrate that the sign structure of the spatial operator is not merely a technical detail, but rather a fundamental feature determining both the qualitative and quantitative behavior of the problem. Studies on traveling waves and related closed-form solutions for nonlinear hyperbolic Schrödinger equations [8, 9] also indicate that the indefinite structure requires different technical approaches; however, this literature does not overlap with the systematic numerical analysis of linear variable-coefficient initial–boundary value problems.

On the numerical side, the Crank–Nicolson discretization continues to be one of the most widely used methods for Schrödinger equations because of its second-order accuracy in time and its implicit

structure [11]. In terms of the theory of consistency, stability, and convergence of finite difference schemes, Morton and Mayers [12] and Strikwerda [13] provide the principal standard references. Among studies more closely related to Schrödinger problems, Antonopoulou, Karali, Plexousakis, and Zouraris [14] obtained optimal-order error estimates for a Crank–Nicolson-based finite element discretization of a two-dimensional linear Schrödinger equation, while Gordin and Tsymbalov [15] developed high-order compact difference schemes for variable-coefficient parabolic and Schrödinger equations. The numerical approaches proposed by Modanli et al. [16] for Schrödinger parabolic and pseudoparabolic equations likewise highlight the importance of discretization design and stability analysis for this class of problems. Nevertheless, most of these works focus either on lower-dimensional settings or on different geometries and operator classes.

From the viewpoint of code verification and error analysis, the method of manufactured solutions, systematized by Roache, provides an established framework for quantitatively evaluating discretization error [17]. This approach is particularly useful in numerical verification studies because it allows the orders of convergence in time and space to be tested independently. In addition, when data or boundary values are affected by measurement errors, Monte Carlo-based approaches provide a natural computational framework for examining the propagation of noise through the numerical scheme [18, 19]. Related finite difference-based reconstruction strategies have also been developed for inverse source problems governed by kinetic and transport-type equations. In this direction, Gölgeleyen, Gölgeleyen, and Hasdemir [20] proposed a hybrid algorithm for a general transport equation, while Gölgeleyen, Hasdemir, and Kaytmaz [21] considered a kinetic inverse source problem with gradient-type boundary data. Hasdemir, Gölgeleyen, and Kaytmaz [22] further extended the kinetic inverse source framework to equations with absorption and scattering terms by combining finite difference approximations, interpolation-based reconstruction, regularization, and Monte Carlo noise sensitivity analysis.

Recent studies have also addressed stability and uniqueness issues for hyperbolic and ultrahyperbolic Schrödinger-type equations. Global and local Carleman estimates have been used to derive Hölder and conditional stability results for inverse and Cauchy problems involving the ultrahyperbolic Schrödinger equation [23, 24]. In addition, uniqueness for a Cauchy problem for a generalized Schrödinger equation in an unbounded domain was established via semigeodesic coordinates and a pointwise Carleman estimate [25].

The hyperbolic character of $\mathcal{L}$ also has direct consequences for the numerical analysis and explains why results developed for the classical elliptic Schrödinger equation cannot be transferred directly. In the elliptic case, the spatial operator is associated with the sign-definite quadratic form

$$\int_{\Omega}(-\Delta w)\overline{w}\,d\mathbf{x} = \|\nabla w\|_{L^2}^2 \geq 0,$$

so coercivity and elliptic regularity provide standard tools for stability and error estimates. In the present setting, however,

$$\int_{\Omega}(-\mathcal{L}w)\overline{w}\,d\mathbf{x} = \|w_y\|_{L^2}^2 - \|w_{x_1}\|_{L^2}^2 - \|w_{x_2}\|_{L^2}^2$$

is indefinite, and the corresponding spatial symbol changes sign and vanishes on a nontrivial characteristic cone. Consequently, although Crank–Nicolson time stepping and central spatial

differences can still be adapted to the problem, coercivity-based stability and convergence arguments from the elliptic setting cannot be transferred verbatim, particularly in the presence of a variable coefficient [13, 14].

Although variable-coefficient Schrödinger equations, indefinite spatial operators, and numerical schemes for Schrödinger-type problems have each been studied extensively, their combination within a three-dimensional variable-coefficient hyperbolic Schrödinger initial–boundary value problem has received comparatively little attention. These difficulties may partly explain this scarcity: the lack of a coercive spatial structure makes rigorous stability and error estimates more problem-dependent, especially for variable coefficients. In addition, constructing exact benchmark solutions compatible with variable coefficients and bounded-domain data can be difficult, which makes the method of manufactured solutions particularly useful for code verification [17]. This gap motivates the present study, in which a finite difference framework is developed and analyzed for such a problem.

The main contribution of this work is the construction and analysis of a Crank–Nicolson finite difference method for a three-dimensional variable-coefficient hyperbolic Schrödinger initial–boundary value problem with an indefinite spatial operator. The scheme combines trapezoidal time averaging with second-order central differences in all three spatial directions and yields a sparse complex linear system whose coefficient matrix is time-independent, so that a single sparse factorization can be reused throughout the time stepping. The local truncation error is shown to be of second order in time and space. Under the frozen-coefficient assumption, the von Neumann analysis yields an amplification factor of unit modulus for all wave numbers and time steps. For the variable-coefficient Dirichlet problem, a discrete weighted-energy argument establishes exact conservation of the a-weighted discrete L^2-norm for the homogeneous perturbation equation and, when combined with consistency, yields a second-order convergence estimate in the discrete L^2-norm without additional stability assumptions. In both arguments the indefinite sign structure enters only through the sign of a real quantity—the discrete spatial symbol in the frozen-coefficient case and the quadratic form associated with L_h in the variable-coefficient case—and only the reality of that quantity, not its sign, is used. Finally, the convergence behavior of the method is examined independently in time and space using manufactured solutions, and its robustness with respect to perturbed data is assessed through Monte Carlo experiments with additive complex Gaussian noise. The continuous problem and its uniqueness result are included to specify the analytical setting of the problem approximated by the numerical scheme.

The remainder of this paper is organized as follows. In Section 2, the initial–boundary value problem for the Schrödinger-type equation under consideration is formulated, and a uniqueness result is presented. In Section 3, the numerical solution algorithm is described in detail. In Section 4, the consistency, stability, and convergence analysis of the proposed scheme is given. In Section 5, numerical results obtained within the framework of the manufactured solution method are presented to support the analytical and numerical observations. Finally, in Section 6, the main results are summarized and several directions for future work are outlined.

2. Problem formulation and uniqueness

We now formulate the initial–boundary value problem associated with Eq (1.1). Throughout the paper, we adopt the standard subscript notation for partial derivatives:

$$z_t = \partial_t z, \qquad z_{x_j x_j} = \partial_{x_j}^2 z \quad (j = 1, 2), \qquad z_{yy} = \partial_y^2 z.$$

Problem 2.1. *Given a source term f, an initial datum z_0, and boundary data g, find a complex-valued function*

$$z : \overline{\Omega_T} \to \mathbb{C}$$

satisfying Eq (1.1)*, together with the initial condition*

$$z(0, \mathbf{x}) = z_0(\mathbf{x}), \qquad \mathbf{x} \in \Omega, \tag{2.1}$$

and the Dirichlet boundary condition

$$z(t, \mathbf{x}) = g(t, \mathbf{x}), \qquad (t, \mathbf{x}) \in \partial\Omega \times (0, T). \tag{2.2}$$

We additionally impose the natural compatibility condition

$$z_0(\mathbf{x}) = g(0, \mathbf{x}), \qquad \mathbf{x} \in \partial\Omega, \tag{2.3}$$

to ensure consistency between the initial and boundary data.

Theorem 2.1. *Assume that $a = a(x_1, x_2)$ is real-valued and satisfies*

$$0 < a_0 \le a(x_1, x_2) \le a_1 < \infty, \qquad (x_1, x_2) \in [x_{1,\min}, x_{1,\max}] \times [x_{2,\min}, x_{2,\max}], \tag{2.4}$$

for some positive constants a_0 and a_1. Then, for any prescribed data (f, z_0, g), Problem 2.1 admits at most one solution in the class

$$\mathcal{Z}(\Omega_T) := H^1(0, T; L^2(\Omega)) \cap L^2(0, T; H^2(\Omega)), \tag{2.5}$$

satisfying the equation, initial condition, and boundary condition in the strong sense. In particular, the Dirichlet boundary datum g is not required to vanish.

Proof. Let $z_1, z_2 \in \mathcal{Z}(\Omega_T)$ be two solutions corresponding to the same data (f, z_0, g), and set $w = z_1 - z_2$. Then

$$\mathcal{S}w = 0, \qquad w(0, \cdot) = 0, \qquad w|_{\partial\Omega\times(0,T)} = 0,$$

regardless of whether g is homogeneous. Hence $w(t, \cdot) \in H^2(\Omega) \cap H_0^1(\Omega)$ for almost every $t \in (0, T)$. Multiplying $\mathcal{S}w = 0$ by a to obtain $aw_t + i\mathcal{L}w = 0$, multiplying by $\overline{w}$, integrating over Ω, and taking real parts gives

$$\frac{1}{2}\frac{d}{dt}\int_\Omega a|w|^2 \, d\mathbf{x} = 0,$$

where we used that a is real-valued and independent of t, and that integration by parts yields

$$\int_\Omega (\mathcal{L}w)\overline{w} \, d\mathbf{x} = -\|w_y\|_{L^2}^2 + \|w_{x_1}\|_{L^2}^2 + \|w_{x_2}\|_{L^2}^2 \in \mathbb{R}.$$

Because $w(0, \cdot) = 0$ and $a \ge a_0 > 0$, it follows that $w \equiv 0$, and therefore $z_1 = z_2$. □

Remark 2.1. *The indefinite sign structure of $\mathcal{L}$ does not affect this uniqueness argument: only the reality of the quadratic form*

$$-\|w_y\|_{L^2}^2 + \|w_{x_1}\|_{L^2}^2 + \|w_{x_2}\|_{L^2}^2$$

is used, not its sign. Note also that the conserved quantity is the squared a-weighted L^2-norm rather than the plain squared L^2-norm.

For the classical constant-coefficient case $\mathcal{L} = \Delta$, $a \equiv 1$, the identity above reduces to the familiar L^2 conservation law; see, for example, [2].

3. Numerical algorithm

In this section, we describe the Crank–Nicolson finite difference scheme used to compute approximate solutions to Problem 2.1. We first introduce the spatial and temporal grids, then derive the discrete equations, and finally present the assembly of the resulting linear system in matrix form.

3.1. Discretization grid

Let $N_{x_1}, N_{x_2}, N_y \in \mathbb{N}$ denote the number of grid points in the x_1-, x_2-, and y-directions, respectively, and let $N_t \in \mathbb{N}$ denote the number of time steps. The corresponding uniform grid spacings are

$$h_{x_1} = \frac{x_{1,\max} - x_{1,\min}}{N_{x_1} - 1}, \quad h_{x_2} = \frac{x_{2,\max} - x_{2,\min}}{N_{x_2} - 1}, \quad h_y = \frac{y_{\max} - y_{\min}}{N_y - 1}, \quad \Delta t = \frac{T}{N_t}. \tag{3.1}$$

The grid nodes are defined by

$$x_{1,j} = x_{1,\min} + (j-1)\,h_{x_1}, \quad x_{2,k} = x_{2,\min} + (k-1)\,h_{x_2}, \quad y_r = y_{\min} + (r-1)\,h_y, \quad t^n = n\,\Delta t, \tag{3.2}$$

for $j = 1, \ldots, N_{x_1}$, $k = 1, \ldots, N_{x_2}$, $r = 1, \ldots, N_y$, and $n = 0, 1, \ldots, N_t$. We denote the discrete approximation of $z(t^n, x_{1,j}, x_{2,k}, y_r)$ by $z^n_{j,k,r}$, and similarly $f^n_{j,k,r} := f(t^n, x_{1,j}, x_{2,k}, y_r)$ and $a_{j,k} := a(x_{1,j}, x_{2,k})$. The set of interior indices is

$$\mathcal{I} := \{(j,k,r) : 2 \le j \le N_{x_1} - 1,\ 2 \le k \le N_{x_2} - 1,\ 2 \le r \le N_y - 1\},$$

and its complement on the boundary $\partial\Omega$ is denoted by $\mathcal{B}$.

3.2. Finite difference operators

The temporal and spatial derivatives are approximated using standard finite differences. For the time derivative, we use the forward difference

$$(z_t)^{n+1/2}_{j,k,r} \approx \frac{z^{n+1}_{j,k,r} - z^n_{j,k,r}}{\Delta t}, \tag{3.3}$$

which provides a second-order accurate approximation at the midpoint $t^{n+1/2} := t^n + \Delta t/2$. For the second-order spatial derivatives, we employ the standard central differences

$$(z_{x_1x_1})^n_{j,k,r} \approx \frac{z^n_{j+1,k,r} - 2z^n_{j,k,r} + z^n_{j-1,k,r}}{h^2_{x_1}}, \tag{3.4}$$

$$(z_{x_2x_2})^n_{j,k,r} \approx \frac{z^n_{j,k+1,r} - 2z^n_{j,k,r} + z^n_{j,k-1,r}}{h^2_{x_2}}, \tag{3.5}$$

$$(z_{yy})^n_{j,k,r} \approx \frac{z^n_{j,k,r+1} - 2z^n_{j,k,r} + z^n_{j,k,r-1}}{h^2_{y}}, \tag{3.6}$$

each of which is second-order accurate in the corresponding spatial variable. The discrete spatial operator $\mathcal{L}_h$, defined as the finite difference analogue of $\mathcal{L}$ in (1.2), acts on grid functions z^n as

$$(\mathcal{L}_h z^n)_{j,k,r} := (z_{yy})^n_{j,k,r} - (z_{x_1x_1})^n_{j,k,r} - (z_{x_2x_2})^n_{j,k,r}. \tag{3.7}$$

3.3. Crank–Nicolson scheme

The Crank–Nicolson method [11] approximates the spatial operator at the midpoint $t^{n+1/2}$ as the average of its values at t^n and t^{n+1}. Applying this principle to Eq (1.1) yields the fully discrete scheme: For each interior index $(j,k,r) \in \mathcal{I}$ and each $n = 0, 1, \ldots, N_t - 1$,

$$\frac{z^{n+1}_{j,k,r} - z^n_{j,k,r}}{\Delta t} + \frac{i\, a^{-1}_{j,k}}{2}\left[(\mathcal{L}_h z^{n+1})_{j,k,r} + (\mathcal{L}_h z^n)_{j,k,r}\right] = \frac{1}{2}(f^{n+1}_{j,k,r} + f^n_{j,k,r}). \tag{3.8}$$

Substituting (3.4)–(3.6) into (3.8) and collecting terms, we obtain

$$\begin{aligned}
&\frac{z^{n+1}_{j,k,r} - z^n_{j,k,r}}{\Delta t} + i\,\alpha_{y,j,k}\left[z^{n+1}_{j,k,r+1} - 2z^{n+1}_{j,k,r} + z^{n+1}_{j,k,r-1} + z^n_{j,k,r+1} - 2z^n_{j,k,r} + z^n_{j,k,r-1}\right] \\
&- i\,\alpha_{x_1,j,k}\left[z^{n+1}_{j+1,k,r} - 2z^{n+1}_{j,k,r} + z^{n+1}_{j-1,k,r} + z^n_{j+1,k,r} - 2z^n_{j,k,r} + z^n_{j-1,k,r}\right] \\
&- i\,\alpha_{x_2,j,k}\left[z^{n+1}_{j,k+1,r} - 2z^{n+1}_{j,k,r} + z^{n+1}_{j,k-1,r} + z^n_{j,k+1,r} - 2z^n_{j,k,r} + z^n_{j,k-1,r}\right] \\
&= \tfrac{1}{2}(f^{n+1}_{j,k,r} + f^n_{j,k,r}),
\end{aligned} \tag{3.9}$$

where the discrete coefficients are defined by

$$\alpha_{y,j,k} := \frac{a^{-1}_{j,k}}{2\,h^2_y}, \qquad \alpha_{x_1,j,k} := \frac{a^{-1}_{j,k}}{2\,h^2_{x_1}}, \qquad \alpha_{x_2,j,k} := \frac{a^{-1}_{j,k}}{2\,h^2_{x_2}}. \tag{3.10}$$

For brevity, we introduce the complex stencil coefficients

$$c_{y,j,k} := i\,\alpha_{y,j,k}, \qquad c_{x_1,j,k} := i\,\alpha_{x_1,j,k}, \qquad c_{x_2,j,k} := i\,\alpha_{x_2,j,k}, \tag{3.11}$$

and define the diagonal coefficient

$$d_{j,k} := \frac{1}{\Delta t} - 2c_{y,j,k} + 2c_{x_1,j,k} + 2c_{x_2,j,k}. \tag{3.12}$$

With this notation, scheme (3.9) can be rearranged as

$$\begin{aligned}
&d_{j,k}\, z^{n+1}_{j,k,r} + c_{y,j,k}\,(z^{n+1}_{j,k,r+1} + z^{n+1}_{j,k,r-1}) - c_{x_1,j,k}\,(z^{n+1}_{j+1,k,r} + z^{n+1}_{j-1,k,r}) - c_{x_2,j,k}\,(z^{n+1}_{j,k+1,r} + z^{n+1}_{j,k-1,r}) \\
&\quad = \tilde{d}_{j,k}\, z^n_{j,k,r} - c_{y,j,k}\,(z^n_{j,k,r+1} + z^n_{j,k,r-1}) + c_{x_1,j,k}\,(z^n_{j+1,k,r} + z^n_{j-1,k,r}) \\
&\quad + c_{x_2,j,k}\,(z^n_{j,k+1,r} + z^n_{j,k-1,r}) + \tfrac{1}{2}(f^{n+1}_{j,k,r} + f^n_{j,k,r}),
\end{aligned} \tag{3.13}$$

where

$$\tilde{d}_{j,k} := \frac{1}{\Delta t} + 2c_{y,j,k} - 2c_{x_1,j,k} - 2c_{x_2,j,k}. \tag{3.14}$$

Equation (3.13) constitutes a seven-point stencil that couples the unknown values at time level $n+1$ on the left-hand side with the known values at time level n on the right-hand side.

3.4. Matrix assembly

To assemble the linear system, we introduce the lexicographic ordering $p : \{1, \dots, N_{x_1}\} \times \{1, \dots, N_{x_2}\} \times \{1, \dots, N_y\} \to \{1, \dots, N\}$, defined by

$$p(j,k,r) := (r-1)\, N_{x_1} N_{x_2} + (k-1)\, N_{x_1} + j, \tag{3.15}$$

where $N := N_{x_1} N_{x_2} N_y$ denotes the total number of grid points. The corresponding global solution vector at time level n is

$$\mathbf{z}^n := \left[z_1^n, z_2^n, \dots, z_N^n\right]^\top \in \mathbb{C}^N, \qquad z^n_{p(j,k,r)} = z^n_{j,k,r}. \tag{3.16}$$

With this ordering, scheme (3.13) can be expressed in matrix form as

$$A\, \mathbf{z}^{n+1} = B\, \mathbf{z}^n + \mathbf{F}^{n+1/2} + \mathbf{g}_\partial^{n,n+1}, \tag{3.17}$$

where the source vector is defined by

$$\mathbf{F}^{n+1/2} := \tfrac{1}{2}(\mathbf{f}^{n+1} + \mathbf{f}^n), \qquad \mathbf{f}^n_{p(j,k,r)} := f^n_{j,k,r}. \tag{3.18}$$

For boundary indices, we set $(\mathbf{F}^{n+1/2})_p = 0$, so that the boundary rows impose only the prescribed Dirichlet data, while $\mathbf{g}_\partial^{n,n+1}$ denotes the boundary contribution vector described in Section 3.5.

The system matrices $A, B \in \mathbb{C}^{N \times N}$ are sparse. Their interior rows share the same stencil structure. For an interior grid point $(j,k,r) \in \mathcal{I}$ with global index $p = p(j,k,r)$, only the neighbours that also belong to $\mathcal{I}$ contribute to the rows of A and B. If a neighbouring point lies on the boundary $\partial\Omega$, its contribution is transferred to the right-hand side through the boundary contribution vector $\mathbf{g}_\partial^{n,n+1}$.

For a boundary grid point $(j,k,r) \in \mathcal{B}$ with global index $p = p(j,k,r)$, the corresponding row of A is replaced by an identity row (i.e., $A_{p,p} = 1$ and $A_{p,q} = 0$ for $q \neq p$), while the corresponding row of B is set entirely to zero. The prescribed boundary value at t^{n+1} is then assigned directly to the right-hand side via $\mathbf{g}_\partial^{n,n+1}$.

The nonzero interior entries of A and B are given by

$$\begin{aligned}
&A_{p,p} = d_{j,k}, && B_{p,p} = \widetilde{d}_{j,k}, && \\
&A_{p,p(j,k,r\pm1)} = c_{y,j,k}, && B_{p,p(j,k,r\pm1)} = -c_{y,j,k}, && (j,k,r\pm1) \in \mathcal{I}, \\
&A_{p,p(j\pm1,k,r)} = -c_{x_1,j,k}, && B_{p,p(j\pm1,k,r)} = c_{x_1,j,k}, && (j\pm1,k,r) \in \mathcal{I}, \\
&A_{p,p(j,k\pm1,r)} = -c_{x_2,j,k}, && B_{p,p(j,k\pm1,r)} = c_{x_2,j,k}, && (j,k\pm1,r) \in \mathcal{I}.
\end{aligned} \tag{3.19}$$

3.5. Treatment of Dirichlet boundary contributions

Since boundary-neighbour entries are omitted from the interior matrix rows, their prescribed Dirichlet values must be transferred explicitly to the right-hand side. For an interior index $(j,k,r) \in \mathcal{I}$ whose neighbour $(j',k',r') \in \mathcal{B}$ lies on the boundary, the prescribed boundary data is denoted by

$$g^n_{j',k',r'} := g(t^n, x_{1,j'}, x_{2,k'}, y_{r'}). \tag{3.20}$$

Following the sign conventions in (3.13), the contribution to the p-th component of $\mathbf{g}^{n,n+1}_{\partial}$ from boundary neighbours of an interior point $(j,k,r) \in \mathcal{I}$ is

$$\begin{aligned}(\mathbf{g}^{n,n+1}_{\partial})_p = & - c_{y,j,k} \sum_{(j',k',r') \in \mathcal{N}^{\partial}_{y}(j,k,r)} (g^{n+1}_{j',k',r'} + g^{n}_{j',k',r'}) + c_{x_1,j,k} \sum_{(j',k',r') \in \mathcal{N}^{\partial}_{x_1}(j,k,r)} (g^{n+1}_{j',k',r'} + g^{n}_{j',k',r'}) \\ & + c_{x_2,j,k} \sum_{(j',k',r') \in \mathcal{N}^{\partial}_{x_2}(j,k,r)} (g^{n+1}_{j',k',r'} + g^{n}_{j',k',r'}).\end{aligned} \tag{3.21}$$

where $\mathcal{N}^{\partial}_{\cdot}(j,k,r)$ denotes the set of boundary neighbours of (j,k,r) along the corresponding direction. For a boundary grid point $(j,k,r) \in \mathcal{B}$, the right-hand side is set directly to the prescribed boundary value at time t^{n+1}:

$$(\mathbf{g}^{n,n+1}_{\partial})_{p(j,k,r)} = g^{n+1}_{j,k,r}, \qquad (j,k,r) \in \mathcal{B}. \tag{3.22}$$

We additionally set $(\mathbf{F}^{n+1/2})_{p(j,k,r)} = 0$ for all boundary indices $(j,k,r) \in \mathcal{B}$, so that the boundary rows of the linear system reduce to $z^{n+1}_p = g^{n+1}_{j,k,r}$ as required.

3.6. Algorithmic summary

The complete numerical procedure is summarized in Algorithm 1. The matrices A and B depend only on the grid spacings, the time step Δt, and the variable coefficient $a(x_1, x_2)$; hence they are assembled once at the beginning of the simulation. At each time step, the right-hand side of (3.17) is updated using the previous solution $\mathbf{z}^n$, the source term values at t^n and t^{n+1}, and the boundary data. The resulting sparse complex linear system is solved efficiently at each time step. As discussed in Remark 3.1, the time-independence of A allows its sparse LU factorization to be computed once and reused throughout the simulation.

Algorithm 1 Crank–Nicolson finite difference solver for Problem 2.1

Require: Computational domain Ω; grid sizes $N_{x_1}, N_{x_2}, N_y, N_t$; final time T; coefficient function a; source f; initial datum z_0; boundary data g.

Ensure: Approximate solution $\mathbf{z}^{N_t} \approx z(T, \cdot)$.

1: Construct grid nodes via (3.2) and compute spacings (3.1).
2: Evaluate $a_{j,k}$ at all interior nodes and compute the stencil coefficients $c_{y,j,k}$, $c_{x_1,j,k}$, $c_{x_2,j,k}$ via (3.11).
3: Assemble the sparse matrices A and B according to (3.19).
4: Compute the sparse LU factorization of A once and store it.
5: Initialize $\mathbf{z}^0$ from the initial datum: $z^0_{p(j,k,r)} = z_0(x_{1,j}, x_{2,k}, y_r)$ for all grid points (j, k, r).
6: **for** $n = 0, 1, \ldots, N_t - 1$ **do**
7: Evaluate $\mathbf{f}^n$ and $\mathbf{f}^{n+1}$ at the grid nodes.
8: Compute the source vector $\mathbf{F}^{n+1/2} = \frac{1}{2}(\mathbf{f}^{n+1} + \mathbf{f}^n)$ and set $(\mathbf{F}^{n+1/2})_p = 0$ for all boundary indices $(j, k, r) \in \mathcal{B}$.
9: Compute the boundary contribution vector $\mathbf{g}_\partial^{n,n+1}$ via (3.21) and (3.22).
10: Form the right-hand side: $\mathbf{b} \leftarrow B\,\mathbf{z}^n + \mathbf{F}^{n+1/2} + \mathbf{g}_\partial^{n,n+1}$.
11: Solve the sparse complex linear system $A\,\mathbf{z}^{n+1} = \mathbf{b}$ using the precomputed LU factorization.
12: **end for**
13: **return** $\mathbf{z}^{N_t}$.

Remark 3.1. *The matrix A is sparse with at most seven nonzero entries per interior row, yielding a total of $O(N)$ nonzero elements. Since A is constant in time, its sparse LU factorization is computed once and reused at every time step. Consequently, each time step requires only the update of the right-hand side and a forward/backward substitution, which significantly reduces the per-step computational cost compared to assembling and factorizing the system at each time step.*

4. Stability and convergence analysis

In this section, we analyze the consistency, stability, and convergence of the Crank–Nicolson scheme (3.8). The analysis is carried out within the standard finite difference framework [12, 13]. We first establish the local truncation error of the scheme, then derive a stability estimate via von Neumann analysis under a frozen-coefficient assumption together with a weighted-energy stability estimate for the variable-coefficient Dirichlet problem, and finally combine these results to obtain the convergence rate of the method.

Throughout the analysis, we use the discrete L^2-norm on the grid, defined for any grid function $\mathbf{v} = (v_{j,k,r}) \in \mathbb{C}^N$ by

$$\|\mathbf{v}\|_h^2 := h_{x_1}\, h_{x_2}\, h_y \sum_{j=1}^{N_{x_1}} \sum_{k=1}^{N_{x_2}} \sum_{r=1}^{N_y} \left| v_{j,k,r} \right|^2. \tag{4.1}$$

This norm is the standard discrete analogue of the continuous $L^2(\Omega)$-norm, and its square corresponds to the Riemann sum approximation of $\int_\Omega |v|^2\, d\mathbf{x}$ on the uniform grid.

4.1. Consistency of the scheme

The local truncation error (LTE) of the scheme (3.8) measures the residual obtained when the exact solution $z(t, \mathbf{x})$ of Problem 2.1 is substituted into the discrete equation. Specifically, for an interior grid point $(j, k, r) \in \mathcal{I}$ and time level n, the LTE is defined by

$$\tau_{j,k,r}^{n+1/2} := \frac{z(t^{n+1}, \mathbf{x}_{j,k,r}) - z(t^n, \mathbf{x}_{j,k,r})}{\Delta t} + \frac{i\, a_{j,k}^{-1}}{2}[(\mathcal{L}_h z)(t^{n+1}, \mathbf{x}_{j,k,r}) + (\mathcal{L}_h z)(t^n, \mathbf{x}_{j,k,r})] - \tfrac{1}{2}(f_{j,k,r}^{n+1} + f_{j,k,r}^n), \quad (4.2)$$

where $\mathbf{x}_{j,k,r} := (x_{1,j}, x_{2,k}, y_r)$.

For the truncation error analysis, we assume that the exact solution z and the source term f are sufficiently smooth so that all partial derivatives appearing in the Taylor expansions below are continuous and bounded on $\overline{\Omega_T}$. In particular, the temporal expansion of the discrete time difference involves z_{ttt}, the central difference expansions involve fourth-order spatial derivatives of z, and the midpoint expansion of the source term involves f_{tt}.

Theorem 4.1. *Let z be the exact solution of Problem 2.1 satisfying the smoothness assumption stated in the preceding paragraph. Then the local truncation error of scheme* (3.8) *satisfies*

$$\left|\tau_{j,k,r}^{n+1/2}\right| \le C(\Delta t^2 + h_{x_1}^2 + h_{x_2}^2 + h_y^2), \qquad (j, k, r) \in \mathcal{I}, \quad (4.3)$$

where $C > 0$ depends on the sup-norms of z_{ttt}, the fourth-order spatial derivatives of z, and f_{tt} over $\overline{\Omega_T}$, and on the sup-norm of a^{-1} over $\overline{\Omega}$.

Proof. We expand each term in (4.2) around the midpoint $(t^{n+1/2}, \mathbf{x}_{j,k,r})$ using Taylor's theorem, exploiting the smoothness of z (with continuous and bounded derivatives up to fourth order in space and third order in time) and of f (with continuous and bounded second-order time derivatives) on $\overline{\Omega_T}$.

The discrete time difference, when expanded about the midpoint $t^{n+1/2}$, satisfies

$$\frac{z(t^{n+1}, \mathbf{x}) - z(t^n, \mathbf{x})}{\Delta t} = z_t(t^{n+1/2}, \mathbf{x}) + \frac{\Delta t^2}{24} z_{ttt}(t^{n+1/2}, \mathbf{x}) + O(\Delta t^4). \quad (4.4)$$

Each second-order central difference satisfies the standard expansion

$$\frac{w(\xi + h) - 2w(\xi) + w(\xi - h)}{h^2} = w''(\xi) + \frac{h^2}{12} w^{(4)}(\xi) + O(h^4) \quad (4.5)$$

for any sufficiently smooth function w. Applying (4.5) to each spatial direction and combining the contributions, we obtain

$$(\mathcal{L}_h z)(t, \mathbf{x}_{j,k,r}) = (\mathcal{L} z)(t, \mathbf{x}_{j,k,r}) + \mathcal{R}_h(t, \mathbf{x}_{j,k,r}), \quad (4.6)$$

where the spatial truncation remainder satisfies

$$\left|\mathcal{R}_h(t, \mathbf{x}_{j,k,r})\right| \le \frac{1}{12}\Big(h_y^2 \, \|z_{yyyy}\|_\infty + h_{x_1}^2 \, \|z_{x_1x_1x_1x_1}\|_\infty + h_{x_2}^2 \, \|z_{x_2x_2x_2x_2}\|_\infty\Big) + O(h_{\max}^4), \quad (4.7)$$

with $h_{\max} := \max\{h_{x_1}, h_{x_2}, h_y\}$, where $\|\cdot\|_\infty$ denotes the sup-norm over $\overline{\Omega_T}$, and the $O(h_{\max}^4)$ remainder collects the higher-order terms from each of the central difference expansions.

The Crank–Nicolson averaging in time, combined with a Taylor expansion of $\mathcal{L}_h z$ around $t^{n+1/2}$, yields

$$\tfrac{1}{2}\big[(\mathcal{L}_h z)(t^{n+1},\cdot) + (\mathcal{L}_h z)(t^{n},\cdot)\big] = (\mathcal{L}z)(t^{n+1/2},\cdot) + \tfrac{\Delta t^2}{8}(\mathcal{L}z)_{tt}(t^{n+1/2},\cdot) + \mathcal{R}_h(t^{n+1/2},\cdot) + O(\Delta t^4 + h_{\max}^4). \quad (4.8)$$

The trapezoidal-type average of the source term satisfies

$$\tfrac{1}{2}(f^{n+1} + f^{n}) = f(t^{n+1/2},\cdot) + \frac{\Delta t^2}{8} f_{tt}(t^{n+1/2},\cdot) + O(\Delta t^4). \quad (4.9)$$

Substituting (4.4), (4.8), and (4.9) into (4.2), the leading-order terms cancel by virtue of the fact that the exact solution satisfies $z_t + i\,a^{-1}\,\mathcal{L}z = f$ at every interior point. The remaining second-order residual reads

$$\tau_{j,k,r}^{n+1/2} = \frac{\Delta t^2}{24} z_{ttt} + \frac{i\,a_{j,k}^{-1}\,\Delta t^2}{8}(\mathcal{L}z)_{tt} - \frac{\Delta t^2}{8} f_{tt} + i\,a_{j,k}^{-1}\,\mathcal{R}_h + O(\Delta t^4 + h_{\max}^4),$$

where all derivatives are evaluated at $(t^{n+1/2}, \mathbf{x}_{j,k,r})$.

Differentiating the partial differential equation twice with respect to time, and using the fact that $a = a(x_1, x_2)$ is independent of time, yields the identity

$$f_{tt} = z_{ttt} + i\,a^{-1}\,(\mathcal{L}z)_{tt}. \quad (4.10)$$

Substituting (4.10) into the residual cancels the $(\mathcal{L}z)_{tt}$ term and combines the z_{ttt} contributions:

$$\frac{\Delta t^2}{24} z_{ttt} - \frac{\Delta t^2}{8} z_{ttt} = \left(\frac{1}{24} - \frac{1}{8}\right)\Delta t^2\, z_{ttt} = -\frac{\Delta t^2}{12} z_{ttt}.$$

Hence,

$$\tau_{j,k,r}^{n+1/2} = -\frac{\Delta t^2}{12} z_{ttt}(t^{n+1/2}, \mathbf{x}_{j,k,r}) + i\,a_{j,k}^{-1}\,\mathcal{R}_h(t^{n+1/2}, \mathbf{x}_{j,k,r}) + O(\Delta t^4 + h_{\max}^4). \quad (4.11)$$

Taking absolute values and using the boundedness of a^{-1} on $\overline{\Omega}$ together with (4.7), we obtain the estimate (4.3) with

$$C = C\Big(\|z_{ttt}\|_{L^\infty(\Omega_T)}, \|z_{x_1x_1x_1x_1}\|_{L^\infty(\Omega_T)}, \|z_{x_2x_2x_2x_2}\|_{L^\infty(\Omega_T)}, \|z_{yyyy}\|_{L^\infty(\Omega_T)}, \|a^{-1}\|_{L^\infty(\Omega)}\Big).$$

This completes the proof. □

Theorem 4.1 shows that the scheme is consistent of order $O(\Delta t^2 + h^2)$, where $h^2 := h_{x_1}^2 + h_{x_2}^2 + h_y^2$, confirming the second-order accuracy of the Crank–Nicolson discretization in both time and space.

4.2. Stability estimate

To investigate stability, we apply von Neumann analysis under the frozen-coefficient assumption, following the standard finite difference stability framework [26, 27]. Specifically, we replace the variable coefficient $a(x_1, x_2)$ by a representative constant value $a_\star \in [a_0, a_1]$, where a_0 and a_1 are the lower and upper bounds of a on $\overline{\Omega}$, and analyze the amplification factor of the resulting constant-coefficient scheme on a uniform grid extended periodically over $\mathbb{R}^3$. Although the original problem

is posed on a bounded domain with variable coefficients and Dirichlet boundary conditions, the frozen-coefficient analysis provides a useful local description of the amplification mechanism [13]. A global Fourier-mode argument is not available in the variable-coefficient setting because the Fourier modes no longer diagonalize the discrete spatial operator. Nevertheless, for the present positive and time-independent coefficient, a rigorous global stability estimate can be obtained through a discrete weighted-energy argument, as shown in Remark 4.2.

Consider a discrete plane-wave solution of the form

$$z_{j,k,r}^{n} = G^{n}\, e^{i(\xi_1 x_{1,j} + \xi_2 x_{2,k} + \eta\, y_r)}, \tag{4.12}$$

where $G \in \mathbb{C}$ is the amplification factor and $(\xi_1, \xi_2, \eta) \in \mathbb{R}^3$ is the wave vector. Substituting (4.12) into scheme (3.8) with $a_{j,k}$ replaced by $a_\star$, and using the identity $e^{i\theta h} - 2 + e^{-i\theta h} = -4\sin^2(\theta h/2)$ for each spatial direction, we obtain

$$G - 1 = -i\, a_\star^{-1}\, \frac{\Delta t}{2}\, \mu(\xi_1, \xi_2, \eta)\, (G + 1), \tag{4.13}$$

where the discrete spatial symbol is

$$\mu(\xi_1, \xi_2, \eta) := -\frac{4\sin^2(\eta\, h_y/2)}{h_y^2} + \frac{4\sin^2(\xi_1\, h_{x_1}/2)}{h_{x_1}^2} + \frac{4\sin^2(\xi_2\, h_{x_2}/2)}{h_{x_2}^2}. \tag{4.14}$$

The sign structure of μ reflects the indefinite character of the continuous operator $\mathcal{L}$: the contribution from the y-direction enters with a negative sign, while those from the x_1- and x_2-directions enter positively.

Solving (4.13) for G, we obtain the closed-form expression

$$G = \frac{1 - i\, a_\star^{-1}\, \mu\, \Delta t/2}{1 + i\, a_\star^{-1}\, \mu\, \Delta t/2}. \tag{4.15}$$

Theorem 4.2. *Under the frozen-coefficient assumption, the Crank–Nicolson scheme* (3.8) *is unconditionally stable in the von Neumann sense [13]. Specifically, the amplification factor G defined in* (4.15) *satisfies*

$$|G(\xi_1, \xi_2, \eta)| = 1 \qquad \textit{for all } (\xi_1, \xi_2, \eta) \in \mathbb{R}^3 \textit{ and all } \Delta t > 0. \tag{4.16}$$

Proof. Since $\mu(\xi_1, \xi_2, \eta) \in \mathbb{R}$ and $a_\star > 0$, the quantity $a_\star^{-1}\, \mu\, \Delta t/2$ is real. The amplification factor in (4.15) therefore takes the form $G = (1 - i\beta)/(1 + i\beta)$ with $\beta \in \mathbb{R}$. Computing the modulus,

$$|G|^2 = \frac{|1 - i\beta|^2}{|1 + i\beta|^2} = \frac{1 + \beta^2}{1 + \beta^2} = 1,$$

which yields $|G| = 1$ for all wave numbers and all time steps. □

Remark 4.1. *The discrete symbol* (4.14) *reflects the indefinite character of the continuous operator $\mathcal{L}$: the contribution from the y-direction enters with a negative sign, while the contributions from the x_1- and x_2-directions enter positively. As a consequence, $\mu(\xi_1, \xi_2, \eta)$ may attain both positive and negative values on the discrete frequency domain. Nevertheless, since the imaginary unit i multiplies the real discrete spatial symbol, the amplification factor becomes a quotient of complex conjugates. Therefore, the modulus identity $|G| = 1$ holds regardless of the sign of μ.*

The identity $|G| = 1$ implies that the discrete L^2-norm of the solution is preserved at every time step in the constant-coefficient periodic setting:

$$\|\mathbf{z}^{n+1}\|_h = \|\mathbf{z}^n\|_h, \qquad n = 0, 1, \ldots, N_t - 1. \tag{4.17}$$

Remark 4.2. *Theorem 4.2 establishes norm preservation for the frozen-coefficient periodic problem. For the variable-coefficient Dirichlet problem, Fourier modes no longer diagonalize the discrete operator; nevertheless, the required global stability estimate follows from the following weighted-energy argument. Let D_a denote the diagonal matrix containing the values $a_{j,k}$ at the interior grid points, repeated in the y-direction, and let L_h denote the matrix representation of $\mathcal{L}_h$ restricted to the interior grid. For interior grid functions satisfying homogeneous Dirichlet boundary conditions, define*

$$\langle \mathbf{u}, \mathbf{v} \rangle_h := h_{x_1} h_{x_2} h_y \sum_{(j,k,r)\in\mathcal{I}} u_{j,k,r} \overline{v_{j,k,r}}, \qquad \langle \mathbf{u}, \mathbf{v} \rangle_{a,h} := \langle D_a \mathbf{u}, \mathbf{v} \rangle_h, \tag{4.18}$$

together with the induced norm $\|\mathbf{u}\|_{a,h}^2 := \langle \mathbf{u}, \mathbf{u} \rangle_{a,h}$. The homogeneous perturbation equation can be written as

$$D_a \frac{\mathbf{v}^{n+1} - \mathbf{v}^n}{\Delta t} + \frac{i}{2} L_h (\mathbf{v}^{n+1} + \mathbf{v}^n) = 0. \tag{4.19}$$

Since the grid is uniform in each coordinate direction, L_h is real and symmetric on the interior grid under homogeneous Dirichlet boundary conditions. Taking the inner product $\langle \cdot, \cdot \rangle_h$ of (4.19) *with $\mathbf{v}^{n+1} + \mathbf{v}^n$ and then taking real parts gives*

$$\|\mathbf{v}^{n+1}\|_{a,h} = \|\mathbf{v}^n\|_{a,h}, \qquad n = 0, 1, \ldots, N_t - 1. \tag{4.20}$$

Moreover, the positivity bounds on a imply the norm equivalence

$$a_0^{1/2} \|\mathbf{v}\|_h \le \|\mathbf{v}\|_{a,h} \le a_1^{1/2} \|\mathbf{v}\|_h. \tag{4.21}$$

Consequently,

$$\|\mathbf{v}^n\|_h \le \left(\frac{a_1}{a_0}\right)^{1/2} \|\mathbf{v}^0\|_h, \qquad 0 \le n \le N_t. \tag{4.22}$$

Thus, the stability estimate is a consequence of the positivity and time independence of a and the symmetry of the centered-difference operator; it is not an additional assumption on the initial data.

4.3. Convergence result

We now combine the consistency estimate of Theorem 4.1 with the variable-coefficient weighted stability estimate established in Remark 4.2. A direct estimate of the discrete error recursion then yields the convergence result below.

Let $Z(t^n) := \left(z(t^n, \mathbf{x}_{j,k,r})\right)_{(j,k,r)} \in \mathbb{C}^N$ denote the vector of exact solution values at time level n, and let $\mathbf{z}^n \in \mathbb{C}^N$ denote the numerical solution computed by Algorithm 1. The discrete error vector is

$$\mathbf{e}^n := Z(t^n) - \mathbf{z}^n, \qquad n = 0, 1, \ldots, N_t. \tag{4.23}$$

Theorem 4.3. *Let z be the exact solution of Problem 2.1 satisfying the smoothness assumption of Theorem 4.1, and let $\mathbf{z}^n$ denote the numerical solution produced by Algorithm 1 on the uniform Cartesian grid introduced in Section 3.1, with initial datum $\mathbf{z}^0 = Z(0)$ and exact boundary data. Then the discrete error satisfies*

$$\|\mathbf{e}^n\|_h \le \left(\frac{a_1}{a_0}\right)^{1/2} C\,T(\Delta t^2 + h_{x_1}^2 + h_{x_2}^2 + h_y^2), \qquad 0 \le n \le N_t, \tag{4.24}$$

where $C > 0$ may depend on Ω, the smoothness bounds appearing in Theorem 4.1, and the coefficient bounds, but is independent of Δt, h_{x_1}, h_{x_2}, h_y, and n. In particular, the scheme converges with order $O(\Delta t^2 + h^2)$, where

$$h^2 := h_{x_1}^2 + h_{x_2}^2 + h_y^2.$$

Proof. Introduce the time-scaled matrices

$$\widehat{A} := \Delta t\, A, \qquad \widehat{B} := \Delta t\, B. \tag{4.25}$$

Then the discrete system (3.17) becomes

$$\widehat{A}\mathbf{z}^{n+1} = \widehat{B}\mathbf{z}^n + \Delta t\, \mathbf{F}^{n+1/2} + \Delta t\, \mathbf{g}_\partial^{n,n+1}. \tag{4.26}$$

Substitution of the exact solution values into the discrete equation gives

$$\widehat{A}Z(t^{n+1}) = \widehat{B}Z(t^n) + \Delta t\, \mathbf{F}^{n+1/2} + \Delta t\, \mathbf{g}_\partial^{n,n+1} + \Delta t\, \boldsymbol{\tau}^{n+1/2},$$

where $\boldsymbol{\tau}^{n+1/2}$ is the local truncation error vector and has zero entries at the boundary nodes.

Since exact boundary data are imposed, the discrete error $\mathbf{e}^n = Z(t^n) - \mathbf{z}^n$ vanishes at every boundary node. Subtracting the numerical scheme from the equation satisfied by the exact grid values therefore gives

$$\widehat{A}\mathbf{e}^{n+1} = \widehat{B}\mathbf{e}^n + \Delta t\, \boldsymbol{\tau}^{n+1/2}. \tag{4.27}$$

The boundary rows decouple from the interior rows, so the recursion may be restricted to the interior block. On this block,

$$\widehat{A} = I + \frac{i\Delta t}{2} D_a^{-1} L_h, \qquad \widehat{B} = I - \frac{i\Delta t}{2} D_a^{-1} L_h.$$

For every interior grid vector $\mathbf{w}$,

$$\mathrm{Re}\langle \widehat{A}\mathbf{w}, \mathbf{w}\rangle_{a,h} = \|\mathbf{w}\|_{a,h}^2,$$

because $\mathbf{w}^* L_h \mathbf{w}$ is real. Hence the Cauchy–Schwarz inequality gives

$$\|\widehat{A}\mathbf{w}\|_{a,h} \ge \|\mathbf{w}\|_{a,h}.$$

Thus $\widehat{A}$ is invertible on the interior block and

$$\|\widehat{A}^{-1}\|_{a,h} \le 1. \tag{4.28}$$

Moreover, the weighted conservation identity (4.20) shows that the homogeneous update operator is an isometry:

$$\|\widehat{A}^{-1}\widehat{B}\mathbf{v}\|_{a,h} = \|\mathbf{v}\|_{a,h}. \tag{4.29}$$

Equation (4.27) can therefore be written as

$$\mathbf{e}^{n+1} = \widehat{A}^{-1}\widehat{B}\mathbf{e}^{n} + \Delta t\,\widehat{A}^{-1}\boldsymbol{\tau}^{n+1/2}. \tag{4.30}$$

Taking the weighted norm and using (4.28)–(4.29) yields

$$\|\mathbf{e}^{n+1}\|_{a,h} \le \|\mathbf{e}^{n}\|_{a,h} + \Delta t\,\|\boldsymbol{\tau}^{n+1/2}\|_{a,h}. \tag{4.31}$$

We estimate in $\|\cdot\|_{a,h}$ throughout and pass to $\|\cdot\|_h$ only at the end; converting at every time level would instead introduce the factor $(a_1/a_0)^{1/2}$ once per step.

By Theorem 4.1, (4.21), and the definition of the discrete L^2-norm,

$$\|\boldsymbol{\tau}^{n+1/2}\|_{a,h} \le a_1^{1/2}\|\boldsymbol{\tau}^{n+1/2}\|_h \quad \le a_1^{1/2}C_\tau|\Omega|^{1/2}(\Delta t^2 + h^2),$$

where C_τ is independent of the discretization parameters. Since $\mathbf{e}^0 = \mathbf{0}$, summing (4.31) over the time levels gives

$$\|\mathbf{e}^{n}\|_{a,h} \le \Delta t \sum_{m=0}^{n-1} \|\boldsymbol{\tau}^{m+1/2}\|_{a,h} \quad \le n\Delta t\, a_1^{1/2}C_\tau|\Omega|^{1/2}(\Delta t^2 + h^2) \ \le T\, a_1^{1/2}C_\tau|\Omega|^{1/2}(\Delta t^2 + h^2).$$

Finally, the lower bound in (4.21) gives

$$\|\mathbf{e}^{n}\|_h \le a_0^{-1/2}\|\mathbf{e}^{n}\|_{a,h}.$$

Combining the last two estimates and absorbing $|\Omega|^{1/2}$ into the constant yields (4.24). Since the homogeneous update operator is an isometry in $\|\cdot\|_{a,h}$, the error recursion can be summed directly, and the resulting estimate contains a factor linear in T rather than an exponential one. □

The convergence result of Theorem 4.3 confirms that the proposed Crank–Nicolson scheme achieves second-order accuracy in both time and space, in agreement with the local truncation error analysis of Theorem 4.1. The temporal and spatial convergence behavior is examined independently in Section 5 through systematic numerical experiments.

4.4. Reported error measures

The convergence estimate (4.24) is established in the discrete L^2-norm $\|\cdot\|_h$ defined in (4.1). In the numerical experiments, we report both relative L^2-errors and absolute L^∞-errors in order to assess the accuracy of the proposed scheme from both integral and pointwise perspectives.

For a numerical solution $\mathbf{z}^n$ and the corresponding exact solution vector $Z(t^n)$, the relative discrete L^2-error is defined by

$$E_2^n := \frac{\|\mathbf{e}^n\|_h}{\|Z(t^n)\|_h}, \qquad \mathbf{e}^n = Z(t^n) - \mathbf{z}^n, \tag{4.32}$$

provided that $\|Z(t^n)\|_h$ remains bounded away from zero over the time interval considered.

The absolute discrete L^∞-error is defined by

$$E_\infty^n := \|\mathbf{e}^n\|_{h,\infty} = \max_{\substack{1\le j\le N_{x_1}\\ 1\le k\le N_{x_2}\\ 1\le r\le N_y}} \left|z(t^n, \mathbf{x}_{j,k,r}) - z_{j,k,r}^n\right|. \tag{4.33}$$

In the convergence tables, the observed convergence orders p_2 and p_∞ are computed as the slopes of the best-fit lines in the log–log plots of the error versus the mesh size for spatial refinements, and versus the time step for temporal refinements. These slopes are obtained by least-squares linear regression of $\log E$ with respect to $\log h$ or $\log \Delta t$, using all refinement levels.

4.5. Sensitivity to noisy data

In addition to the deterministic convergence tests, we examine the sensitivity of the proposed scheme to perturbations in the input and observed data. In practical computations, boundary measurements and observed numerical outputs may contain measurement or modelling errors. To assess the effect of such perturbations, a Monte Carlo noise analysis is performed in Section 5.

For a prescribed relative noise level $\delta \in [0, 1]$, additive complex-valued Gaussian noise is introduced through two independent mechanisms [19, 28].

At each time step t^n, the prescribed Dirichlet boundary data are perturbed independently at every boundary node $\mathbf{x}_q \in \partial\Omega$:

$$\widetilde{g}(t^n, \mathbf{x}_q) = g(t^n, \mathbf{x}_q) + \sigma^n_{\text{bnd}}(W_r + iW_i), \tag{4.34}$$

where $W_r, W_i \sim \mathcal{N}(0, 1)$ are independent standard Gaussian random variables and

$$\sigma^n_{\text{bnd}} = \frac{\delta \, \|\mathbf{z}^n\|_2}{\sqrt{2N_\partial}}. \tag{4.35}$$

Here, N_∂ denotes the number of boundary nodes. The perturbed boundary values at t^n and t^{n+1} are generated once per time step and then used consistently in the boundary contribution vector.

At the final time $t = T$, an additional perturbation is applied to the computed solution in order to model measurement noise in the observed numerical output:

$$\widetilde{\mathbf{z}}^{N_t} = \mathbf{z}^{N_t} + \sigma_{\text{obs}}(\boldsymbol{W}_r + i\boldsymbol{W}_i), \qquad \sigma_{\text{obs}} = \frac{\delta \, \|\mathbf{z}^{N_t}\|_2}{\sqrt{2N}}, \tag{4.36}$$

where $\boldsymbol{W}_r, \boldsymbol{W}_i \in \mathbb{R}^N$ have independent standard Gaussian components and N is the total number of grid points.

The scaling factors $\sqrt{2N_\partial}$ and $\sqrt{2N}$ ensure that the expected Euclidean norm of the complex perturbation is proportional to $\delta \, \|\mathbf{z}\|_2$, so that δ represents the prescribed relative noise level. For each $\delta \in \{0\%, 1\%, 5\%, 10\%\}$, $N_{\text{MC}} = 200$ independent realizations are computed, and the mean and standard deviation of the relative L^2- and absolute L^∞-errors are reported. Since the proposed scheme is linear, the induced error is expected to scale approximately linearly with δ for small noise levels, providing a useful reference for interpreting the Monte Carlo results.

5. Numerical experiments

In this section, numerical experiments are presented to verify the accuracy, convergence behavior, and robustness of the proposed numerical algorithm for Problem 2.1. The error measures used in the following tables and figures are defined in Section 4.4. Monte Carlo simulations are performed to examine the sensitivity of the scheme to noisy data, following the perturbation setting described in Section 4.5.

Example 1. *Consider Problem 2.1 on the computational domain*

$$\Omega_1 = [1, 2] \times [-1, 2] \times [1, 3], \qquad t \in (0, T], \qquad T = 1,$$

with the variable coefficient

$$a(x_1, x_2) = 2 + x_1^2 + x_2^2 + \tfrac{1}{4} x_1 x_2,$$

the source function

$$f(x_1, x_2, y, t) = \frac{2\sin(2t)}{x_1^2 + \frac{x_1x_2}{4} + x_2^2 + 2} - e^{-t}(x_1x_2 + 1)\cos\left(\frac{\pi(y-1)}{2}\right) + i\left[2(x_1^2 + x_1x_2 + x_2^2 + y^2)\cos(2t) - \frac{\pi^2 e^{-t}(x_1x_2 + 1)\cos\left(\frac{\pi(y-1)}{2}\right)}{4(x_1^2 + \frac{x_1x_2}{4} + x_2^2 + 2)}\right],$$

the initial condition

$$z_0(\mathbf{x}) = (1 + x_1x_2)\cos\left(\frac{\pi(y-1)}{2}\right),$$

and the Dirichlet boundary data $g(t, \mathbf{x})$ *prescribed on* $\partial\Omega_1 \times (0, T]$.

The exact solution of Example 1 is

$$z(x_1, x_2, y, t) = e^{-t}(1 + x_1x_2)\cos\left(\frac{\pi(y-1)}{2}\right) + i\sin(2t)(x_1^2 + x_2^2 + y^2 + x_1x_2). \tag{5.1}$$

For the main computation, the discretization parameters are taken as

$$\Delta t = 0.01, \qquad N_{x_1} = 10, \quad N_{x_2} = 28, \quad N_y = 19.$$

The spatial convergence test is performed on the grid sequence

$$(5, 13, 9), \quad (9, 25, 17), \quad (17, 49, 33),$$

while the temporal convergence test is carried out on the fixed grid

$$N_{x_1} = 16, \qquad N_{x_2} = 46, \qquad N_y = 31.$$

The relative L^2-error E_2^n and the absolute L^∞-error E_∞^n, defined by (4.32) and (4.33) respectively, are reported in the following tables.

The numerical results indicate that the proposed scheme provides stable and accurate approximations for Example 1. Table 1 and Figures 1–3 show that the numerical solution remains close to the exact solution throughout $(0, T]$, with small and regularly distributed errors. The convergence plots in Figure 4, together with Tables 2 and 3, confirm that the spatial convergence rates are close to the expected second-order behavior, while the temporal rates approach the spatial-discretization plateau for smaller time steps. Finally, Table 4 shows that the mean errors scale approximately linearly with the noise level δ, indicating that the scheme is robust with respect to moderate data perturbations.

Table 1. Errors at selected time levels for Example 1.

t^n	E_2^n	E_∞^n
0.01	6.6186×10^{-6}	3.2751×10^{-5}
0.23	4.8209×10^{-5}	9.2383×10^{-4}
0.45	4.7674×10^{-5}	1.8412×10^{-3}
0.67	5.0288×10^{-5}	2.0416×10^{-3}
0.78	5.3538×10^{-5}	2.1844×10^{-3}
0.89	5.8871×10^{-5}	2.3570×10^{-3}
1.00	6.7465×10^{-5}	2.3972×10^{-3}

Table 2. Temporal convergence results for Example 1 at $t = T$.

Δt	$E_2^{N_t}$	$E_\infty^{N_t}$	CPU time (s)
0.1000	2.5554×10^{-3}	9.4926×10^{-2}	5.8684
0.0500	6.3718×10^{-4}	2.3116×10^{-2}	11.9721
0.0250	1.5759×10^{-4}	5.7827×10^{-3}	24.0201
0.0125	4.4844×10^{-5}	1.5193×10^{-3}	47.6200
0.0063	2.9031×10^{-5}	9.9403×10^{-4}	95.8549
Observed orders: $p_2 = 1.675$, $p_\infty = 1.708$.			

Table 3. Spatial convergence results for Example 1 with $\Delta t = 10^{-3}$.

Grid ($N_{x_1} \times N_{x_2} \times N_y$)	h	$E_2^{N_t}$	$E_\infty^{N_t}$	CPU time (s)
$5 \times 13 \times 9$	0.25000	3.0818×10^{-4}	1.0374×10^{-2}	1.3820
$9 \times 25 \times 17$	0.12500	9.4939×10^{-5}	3.1173×10^{-3}	23.6312
$17 \times 49 \times 33$	0.06250	2.5818×10^{-5}	8.3677×10^{-4}	803.3163
Observed orders: $p_2 = 1.789$, $p_\infty = 1.816$.				

Table 4. Monte Carlo noise sensitivity results for Example 1 at $t = T$, with $N_{\mathrm{MC}} = 200$ realizations per noise level.

δ	mean($E_2^{N_t}$)	std($E_2^{N_t}$)	mean($E_\infty^{N_t}$)	std($E_\infty^{N_t}$)
0%	6.7465×10^{-5}	0	2.3972×10^{-3}	0
1%	1.6503×10^{-2}	1.3998×10^{-4}	4.6592×10^{-1}	3.9783×10^{-2}
5%	8.2742×10^{-2}	7.4727×10^{-4}	2.3471	1.9018×10^{-1}
10%	1.6657×10^{-1}	1.3679×10^{-3}	4.6777	3.8664×10^{-1}

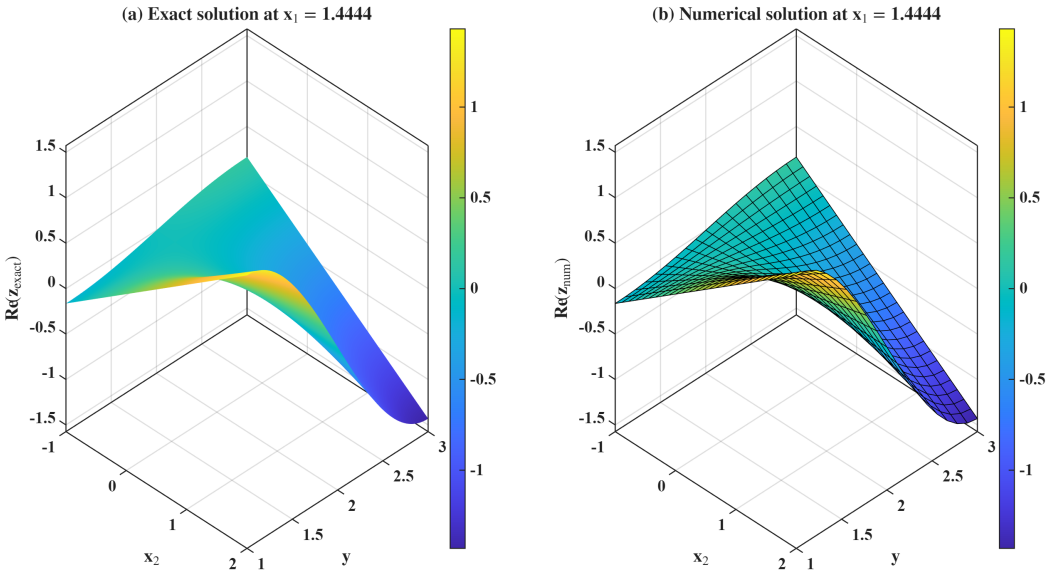

Figure 1. Exact and numerical solutions on the plane $x_1 = x_{1,\mathrm{mid}}$ at $t = T$ for Example 1. The grid lines on the numerical surface indicate the finite difference mesh.

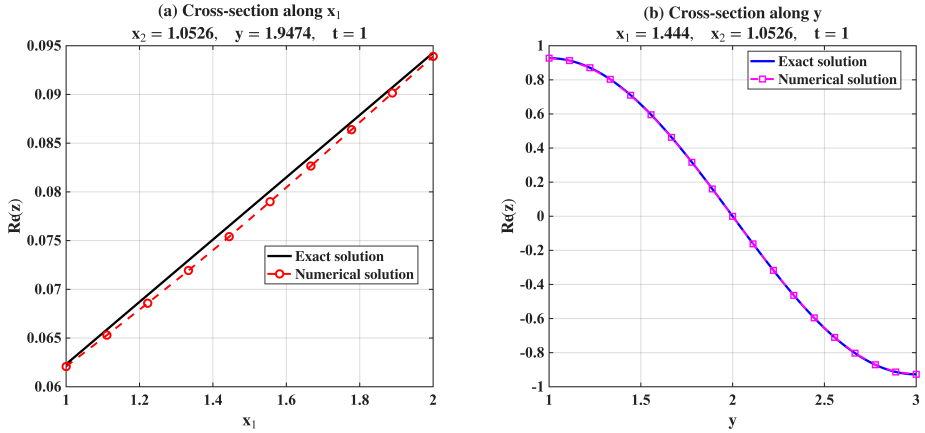

Figure 2. One-dimensional cross-sections of the exact and numerical solutions at $t = T$ for Example 1: (a) along the x_1-direction at $x_2 = x_{2,\text{mid}}$, $y = y_{\text{mid}}$; (b) along the y-direction at $x_1 = x_{1,\text{mid}}$, $x_2 = x_{2,\text{mid}}$.

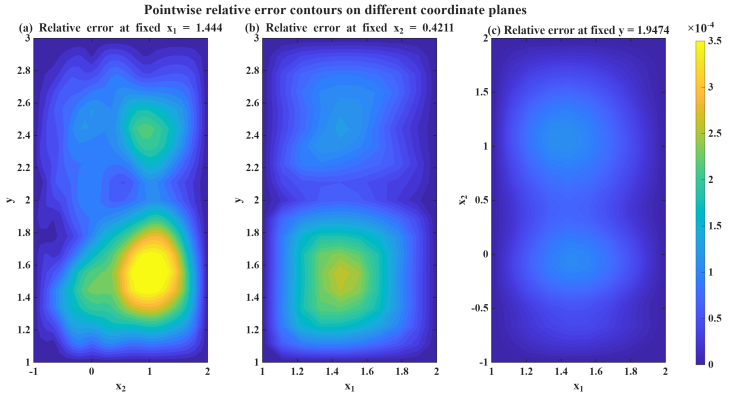

Figure 3. Pointwise relative error distribution on the plane $y = y_{\text{mid}}$ at $t = T$ for Example 1.

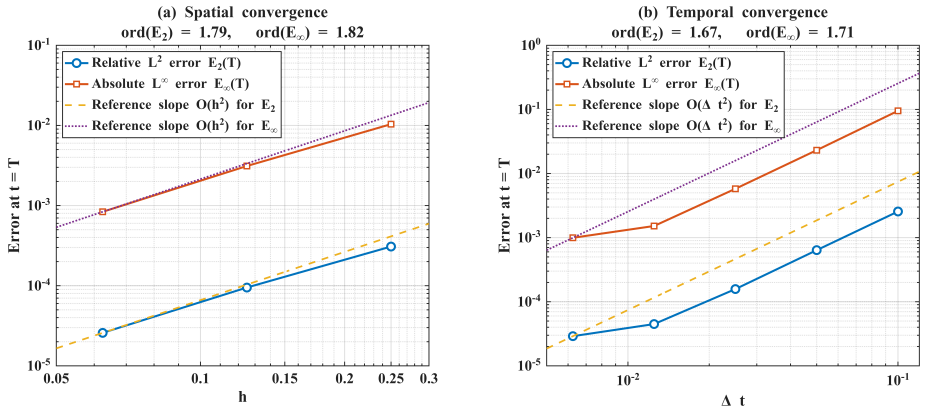

Figure 4. Spatial and temporal convergence behavior of the proposed scheme for Example 1.

Example 2. *Consider Problem 2.1 on the computational domain*

$$\Omega_2 = [0,1] \times [0,2] \times [-1,1], \qquad t \in (0,T], \qquad T = 0.5,$$

with the variable coefficient

$$a(x_1, x_2) = 2 + \cos(\pi x_1)\sin\left(\frac{\pi x_2}{2}\right) + \tfrac{1}{2}(x_1 + x_2^2),$$

the source function

$$\begin{aligned} f(x_1, x_2, y, t) = & -\frac{\sin(2t)\, e^{-(x_1-\frac{1}{2})^2}\sinh(y)\, P(x_1, x_2)}{D(x_1, x_2)} \\ & + i\left[\frac{\cos(2t)\, e^{-t/2}\sin\left(\frac{\pi x_2}{2}\right) Q(x_1, y)}{D(x_1, x_2)} + 2\cos(2t)\, e^{-(x_1-\frac{1}{2})^2}\sinh(y)(x_1^2 x_2 + 1)\right] \\ & - e^{-t/2}\sin\left(\frac{\pi x_2}{2}\right)(x_1 - x_1^2)(y - y^2)\left(\tfrac{1}{2}\cos(2t) + 2\sin(2t)\right), \end{aligned}$$

where

$$D(x_1, x_2) = \frac{x_1}{2} + \cos(\pi x_1)\sin\left(\frac{\pi x_2}{2}\right) + \frac{x_2^2}{2} + 2,$$

$$Q(x_1, y) = 2(y - y^2) - 2(x_1 - x_1^2) + \frac{\pi^2}{4}(x_1 - x_1^2)(y - y^2),$$

$$P(x_1, x_2) = -4x_1^4 x_2 + 4x_1^3 x_2 + 10x_1^2 x_2 - 4x_1^2 - 4x_1 x_2 + 4x_1 - 2x_2 + 2,$$

together with the corresponding initial datum z_0 and Dirichlet boundary data g.

The exact solution of Example 2 is

$$z(x_1, x_2, y, t) = e^{-\alpha t}\cos(\beta t)(x_1 - x_1^2)\sin\left(\frac{\pi x_2}{2}\right)(y - y^2) + i\sin(\beta t)(1 + x_1^2 x_2)\sinh(y)\exp\left[-\left(x_1 - \frac{1}{2}\right)^2\right],$$

with $\alpha = 1/2$ and $\beta = 2$. The real part exhibits both temporal damping and spatial oscillation, while the imaginary part includes hyperbolic and Gaussian-type spatial dependence.

For the variable coefficient $a(x_1, x_2)$, numerical inspection on $\overline{\Omega_2}$ confirms $a_{\min} > 0$, ensuring that the problem is well-defined.

For the main computation, the discretization parameters are taken as

$$\Delta t = 0.020, \qquad N_{x_1} = 9, \quad N_{x_2} = 17, \quad N_y = 9.$$

The spatial convergence test is performed on the grid sequence

$$(5, 9, 5), \quad (9, 17, 9), \quad (17, 33, 17),$$

with $\Delta t = 10^{-3}$. The temporal convergence test is carried out on the fixed grid

$$N_{x_1} = 17, \qquad N_{x_2} = 33, \qquad N_y = 17,$$

using the time-step sequence

$$\Delta t = 0.2500, \quad 0.1250, \quad 0.0625, \quad 0.03125.$$

The numerical results show that the proposed scheme remains stable and accurate for the more challenging Example 2, which involves a damped-oscillatory complex-valued exact solution. Table 5 and Figures 5–7 demonstrate good agreement between the numerical and exact solutions. The convergence results in Figure 8 and Tables 6–7 show decreasing errors under refinement, with temporal rates close to the expected second-order behavior and slightly lower spatial rates due to the more oscillatory hyperbolic–Gaussian structure of the solution. Finally, Table 8 indicates robustness under data perturbations, as the mean errors scale approximately linearly with the noise level δ.

Table 5. Errors at selected time levels for Example 2.

t^n	E_2^n	E_∞^n
0.02	2.6419×10^{-5}	1.4675×10^{-5}
0.12	1.5986×10^{-4}	1.7359×10^{-4}
0.24	3.0011×10^{-4}	6.1885×10^{-4}
0.34	4.0889×10^{-4}	1.0309×10^{-3}
0.40	4.7263×10^{-4}	1.2791×10^{-3}
0.50	5.8010×10^{-4}	1.6689×10^{-3}

Table 6. Temporal convergence results for Example 2 at $t = T$ on the fixed spatial grid $17 \times 33 \times 17$.

Δt	$E_2^{N_t}$	$E_\infty^{N_t}$	CPU (s)
0.2500	1.1258×10^{-2}	2.7129×10^{-2}	0.3338
0.1250	2.8008×10^{-3}	7.1149×10^{-3}	0.5330
0.0625	7.0919×10^{-4}	1.9139×10^{-3}	1.0884
0.03125	2.4189×10^{-4}	6.3231×10^{-4}	2.0898
Observed orders: $p_2 = 1.860$, $p_\infty = 1.816$.			

Table 7. Spatial convergence results for Example 2 with $\Delta t = 10^{-3}$.

Grid ($N_{x_1} \times N_{x_2} \times N_y$)	h	$E_2^{N_t}$	$E_\infty^{N_t}$	CPU (s)
$5 \times 9 \times 5$	0.25000	1.2826×10^{-3}	4.2642×10^{-3}	0.3902
$9 \times 17 \times 9$	0.12500	5.8304×10^{-4}	1.6448×10^{-3}	3.7553
$17 \times 33 \times 17$	0.06250	1.8240×10^{-4}	4.9760×10^{-4}	64.2818
Observed orders: $p_2 = 1.407$, $p_\infty = 1.550$.				

Table 8. Monte Carlo noise sensitivity results for Example 2 at $t = T$, with $N_{\mathrm{MC}} = 200$ realizations per noise level.

δ	mean($E_2^{N_t}$)	std($E_2^{N_t}$)	mean($E_\infty^{N_t}$)	std($E_\infty^{N_t}$)
0%	5.8010×10^{-4}	0	1.6689×10^{-3}	0
1%	1.5024×10^{-2}	2.1587×10^{-4}	3.5980×10^{-2}	3.1088×10^{-3}
5%	7.5333×10^{-2}	1.0512×10^{-3}	1.8033×10^{-1}	1.6428×10^{-2}
10%	1.5120×10^{-1}	1.9572×10^{-3}	3.6255×10^{-1}	3.2528×10^{-2}

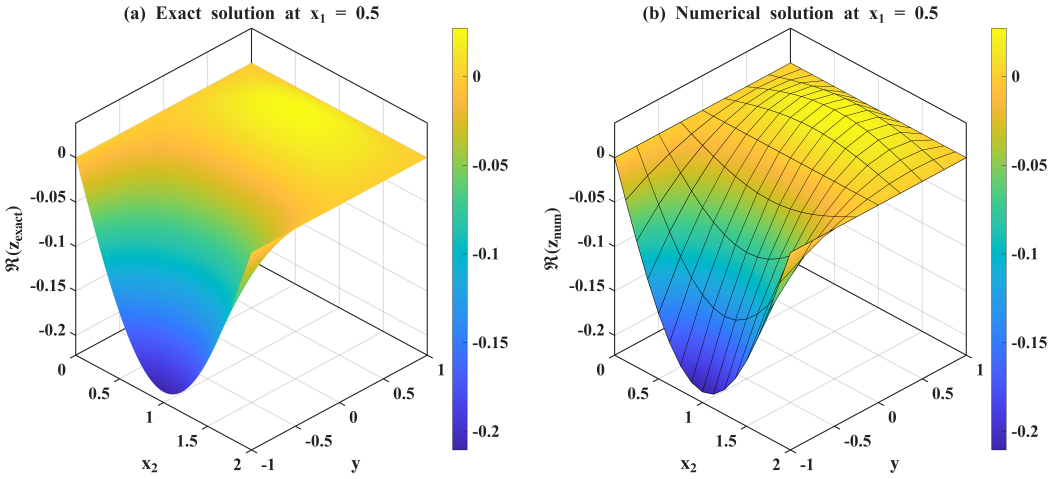

Figure 5. Exact and numerical solutions on the plane $x_1 = x_{1,\text{mid}}$ at $t = T$ for Example 2.

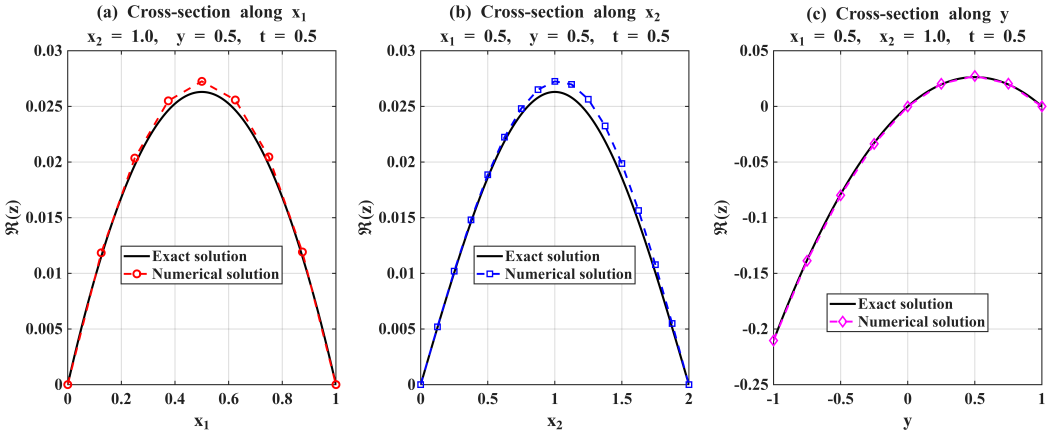

Figure 6. One-dimensional cross-sections of the real parts of the exact and numerical solutions at $t = T$ for Example 2, taken along the x_1-, x_2-, and y-directions.

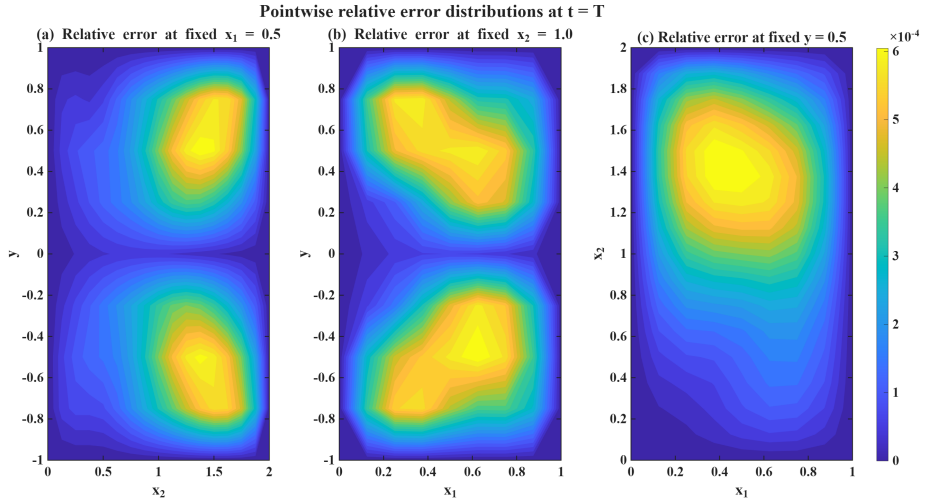

Figure 7. Pointwise relative error distributions on fixed coordinate planes at the final time $t = T$ for Example 2.

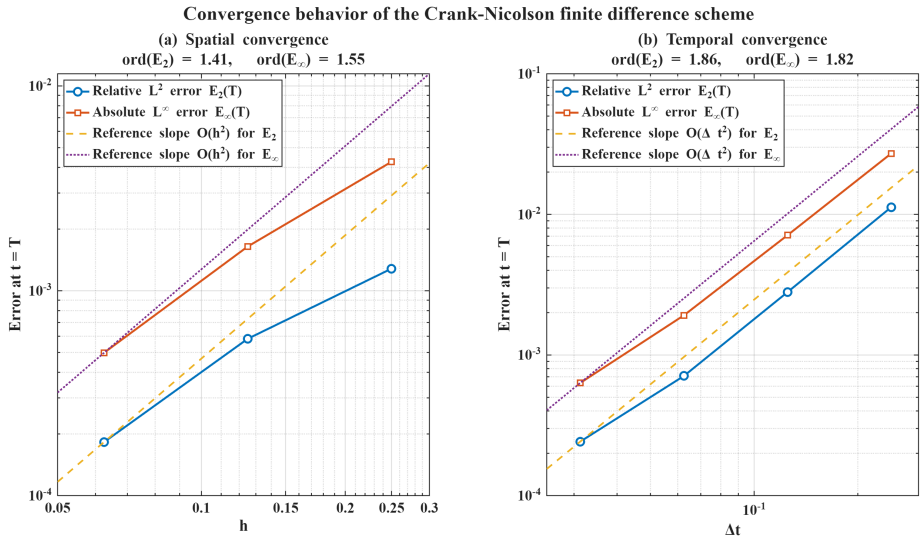

Figure 8. Spatial and temporal convergence behavior of the proposed scheme for Example 2.

6. Conclusions

This paper has developed and analyzed a Crank–Nicolson finite difference method for an initial–boundary value problem governed by a three-dimensional variable-coefficient Schrödinger-type equation. A distinctive feature of the model is the indefinite (hyperbolic) character of its spatial operator, which contains one positive and two negative second-order derivative terms. Under suitable regularity and positivity assumptions on the variable coefficient $a(x_1, x_2)$, a uniqueness theorem was established for the continuous problem, thereby providing the analytical setting for the subsequent numerical treatment.

For the numerical solution, a Crank–Nicolson finite difference scheme was developed by combining trapezoidal time averaging with second-order central spatial differences in all three spatial directions. The resulting discrete problem leads to a sparse complex linear system at each time step. Since the coefficient matrix is time-independent, its sparse factorization can be computed once and reused throughout the time-stepping process.

The consistency, stability, and convergence properties of the proposed scheme were examined within the finite difference framework. The local truncation error analysis establishes second-order consistency in time and space. Under the frozen-coefficient assumption, the von Neumann analysis shows that the amplification factor has unit modulus for every wave number and time step. For the variable-coefficient Dirichlet problem, a discrete weighted-energy argument establishes exact conservation of the weighted norm for the homogeneous perturbation equation and hence uniform stability in the standard discrete L^2-norm. Combining this stability estimate with consistency yields second-order convergence without a time-step restriction.

The numerical results support the analytical findings. Two test problems with prescribed exact solutions were considered on different computational domains, involving complex-valued solutions of varying structure. The temporal and spatial convergence behavior was examined independently and generally supported the predicted trend, with somewhat lower spatial rates for the more oscillatory second example. In addition, Monte Carlo noise sensitivity tests with additive complex Gaussian

perturbations showed that the proposed method remains robust under noisy data.

The continuous uniqueness argument is not intrinsically restricted to rectangular domains. It extends to sufficiently regular solutions on bounded Lipschitz domains for which the trace theorem and Green's identity are valid, since the difference of two solutions with the same Dirichlet data has zero boundary trace and $\int_\Omega (\mathcal{L}w)\overline{w}\, d\mathbf{x}$ remains real. By contrast, the present numerical construction relies on a uniform Cartesian grid and a symmetric seven-point stencil. On an irregular domain, the boundary treatment and spatial discretization must therefore be redesigned, and the consistency and weighted-energy stability arguments must be re-established for the resulting discrete operator.

Future work may focus on nonlinear hyperbolic Schrödinger equations with variable coefficients, higher-order discretizations adapted to the indefinite spatial structure, and extensions to time-dependent coefficients or more general spatial domains. In this context, the generalized finite difference method provides a promising meshless extension of the classical finite difference framework, since it constructs local derivative approximations on arbitrarily scattered nodes and can therefore accommodate complex geometries more naturally [29, 30]. Extending the present method in this direction would require constructing scattered-node approximations of the indefinite spatial operator and establishing the corresponding consistency and weighted-energy stability properties. Another natural direction is the numerical study of inverse and Cauchy problems associated with this class of equations, building on the theoretical stability results [23, 24] and uniqueness results [25] obtained via Carleman estimates and semigeodesic coordinates. The scheme developed in this work could provide an efficient forward solver for such inverse problem investigations.

Author contributions

The author confirms sole responsibility for the conception and design of the study, methodology, analysis, interpretation of results, and manuscript preparation.

Use of Generative-AI tools declaration

The author used AI-assisted tools solely for grammar correction and language editing. All mathematical ideas, results, proofs, and scientific content are entirely the author's original work.

Acknowledgments

The author received no financial support for this research.

Conflict of interest

The author declares no conflict of interest in this paper.

References

1. E. Schrödinger, An undulatory theory of the mechanics of atoms and molecules, *Phys. Rev.,* **28** (1926), 1049–1070. http://dx.doi.org/10.1103/PhysRev.28.1049

2. T. Cazenave, *Semilinear Schrödinger Equations*, Courant Lecture Notes in Mathematics, Vol. 10, New York: American Mathematical Society, 2003.

3. A. Arias Junior, A. Ascanelli, M. Cappiello, C. Garetto, Schrödinger type equations with singular coefficients and lower order terms, *J. Differ. Equations,* **425** (2025), 190–222. http://dx.doi.org/10.1016/j.jde.2025.01.013

4. G. P. Agrawal, *Nonlinear Fiber Optics*, 5 Eds., San Diego: Academic Press, 2013.

5. S. Federico, Z. Li, X. Yu, On the uniqueness of variable coefficient Schrödinger equations, *Commun. Contemp. Math.,* **27** (2025), 2450016. http://dx.doi.org/10.1142/S0219199724500160

6. L. P. Pitaevskii, S. Stringari, *Bose–Einstein Condensation and Superfluidity*, International Series of Monographs on Physics, Vol. 164, Oxford: Oxford University Press, 2016.

7. J. A. Barceló, B. Cassano, L. Fanelli, Unique continuation properties from one time for hyperbolic Schrödinger equations, *SIAM J. Math. Anal.,* **56** (2024), 7417–7438. http://dx.doi.org/10.1137/23M1578218

8. M. R. Ali, M. A. Khattab, S. M. Mabrouk, Investigation of travelling wave solutions for the (3+1)-dimensional hyperbolic nonlinear Schrödinger equation using Riccati equation and F-expansion techniques, *Opt. Quantum Electron.,* **55** (2023), 991. http://dx.doi.org/10.1007/s11082-023-05274-x

9. D. Sherriffe, D. Behera, P. Nagarani, Different forms for exact traveling wave solutions of unstable and hyperbolic nonlinear Schrödinger equations, *Int. J. Mod. Phys. B,* **38** (2024), 2450131. http://dx.doi.org/10.1142/S0217979224501315

10. Ö. Arıbaş, İ. Gölgeleyen, M. Yıldız, Investigation of well-posedness for a direct problem for a nonlinear fractional diffusion equation and an inverse problem, *Fractal Fract.,* **8** (2024), 315. http://dx.doi.org/10.3390/fractalfract8060315

11. J. Crank, P. Nicolson, A practical method for numerical evaluation of solutions of partial differential equations of the heat-conduction type, *Math. Proc. Camb. Philos. Soc.,* **43** (1947), 50–67. http://dx.doi.org/10.1017/S0305004100023197

12. K. W. Morton, D. F. Mayers, *Numerical Solution of Partial Differential Equations: An Introduction*, 2 Eds., Cambridge: Cambridge University Press, 2005. http://dx.doi.org/10.1017/CBO9780511812248

13. J. C. Strikwerda, *Finite Difference Schemes and Partial Differential Equations*, 2 Eds., Philadelphia: SIAM, 2004. http://dx.doi.org/10.1137/1.9780898717938

14. D. C. Antonopoulou, G. D. Karali, M. Plexousakis, G. E. Zouraris, Crank–Nicolson finite element discretizations for a 2D linear Schrödinger-type equation posed in a noncylindrical domain, *Math. Comp.,* **84** (2015), 1571–1598. http://dx.doi.org/10.1090/S0025-5718-2014-02900-1

15. V. A. Gordin, E. A. Tsymbalov, Compact difference scheme for parabolic and Schrödinger-type equations with variable coefficients, *J. Comput. Phys.,* **375** (2018), 1451–1468. http://dx.doi.org/10.1016/j.jcp.2018.06.079

16. M. Modanli, B. Bajjah, S. Kuşulay, Two numerical methods for solving the Schrödinger parabolic and pseudoparabolic partial differential equations, *Adv. Math. Phys.,* **2022** (2022), 6542490. http://dx.doi.org/10.1155/2022/6542490

17. P. J. Roache, Code verification by the method of manufactured solutions, *J. Fluids Eng.,* **124** (2002), 4–10. http://dx.doi.org/10.1115/1.1436090

18. C. P. Robert, G. Casella, *Monte Carlo Statistical Methods*, 2 Eds., New York: Springer, 2004. http://dx.doi.org/10.1007/978-1-4757-4145-2

19. J. Kaipio, E. Somersalo, *Statistical and Computational Inverse Problems*, Applied Mathematical Sciences, Vol. 160, New York: Springer, 2005. http://dx.doi.org/10.1007/b138659

20. F. Gölgeleyen, İ. Gölgeleyen, M. Hasdemir, A hybrid solution method for an inverse problem for the general transport equation, *Comput. Math. Appl.,* **192** (2025), 172–188.

21. İ. Gölgeleyen, M. Hasdemir, Ö. Kaytmaz, A computational approach to an inverse source problem for a kinetic equation with gradient-type boundary data and an interior point observation, *Electron. Res. Arch.,* **34** (2026), 2136–2156.

22. M. Hasdemir, İ. Gölgeleyen, Ö. Kaytmaz, Numerical recovery of unknown source in a kinetic equation with absorption and scattering via an interior measurement, *Electron. Res. Arch.,* **34** (2026), 2774–2804.

23. F. Gölgeleyen, Ö. Kaytmaz, A Hölder stability estimate for inverse problems for the ultrahyperbolic Schrödinger equation, *Anal. Math. Phys.,* **9** (2019), 2171–2199. http://dx.doi.org/10.1007/s13324-019-00336-z

24. İ. Gölgeleyen, Ö. Kaytmaz, Conditional stability for a Cauchy problem for the ultrahyperbolic Schrödinger equation, *Appl. Anal.,* **101** (2022), 1505–1516. http://dx.doi.org/10.1080/00036811.2020.1781829

25. İ. Gölgeleyen, Ö. Kaytmaz, Uniqueness for a Cauchy problem for the generalized Schrödinger equation, *AIMS Math.,* **8** (2023), 5703–5724. http://dx.doi.org/10.3934/math.2023287

26. İ. Gölgeleyen, M. Hasdemir, A solution algorithm for an inverse source problem for the kinetic equation, *Int. J. Mod. Phys. C,* **33** (2022), 2250151. https://doi.org/10.1142/S0129183122501510

27. M. N. Özişik, H. R. Orlande, M. J. Colaço, R. M. Cotta, Finite difference methods in heat transfer, CRC Press, Boca Raton, 2017.

28. C. R. Vogel, *Computational Methods for Inverse Problems*, Frontiers in Applied Mathematics, Vol. 23, Philadelphia: SIAM, 2002. http://dx.doi.org/10.1137/1.9780898717570

29. Z. Sun, H. Wu, J. Li, L. Sun, Generalized finite difference method for anti-plane problems of magnetoelectroelastic materials with inclusions, *Appl. Math. Lett.,* **184** (2026), 110099. http://dx.doi.org/10.1016/j.aml.2026.110099

30. J. Li, S. Yang, X. Wei, L. Sun, Y. Yu, Analysis of plane problems in magneto-electro-elastic media using the generalized finite difference method, *Eng. Anal. Bound. Elem.,* **184** (2026), 106612. http://dx.doi.org/10.1016/j.enganabound.2025.106612

AIMS Press